Controlling activation site density by low-energy far-field stimulation in cardiac tissue

Marcel Hörning,[1,2,*] Seiji Takagi,[3] and Kenichi Yoshikawa[1,4]
[1]*Department of Physics, Graduate School of Science, Kyoto University, Japan*
[2]*Laboratory for Physical Biology, RIKEN Center for Developmental Biology, Kobe 650-0047, Japan*
[3]*Research Institute for Electronic Science, Hokkaido University, Sapporo 060-0812, Japan*
[4]*Life and Medical Sciences, Doshisha University, Kyotanabe City, 610-0394 Japan*
(Received 21 November 2011; revised manuscript received 19 March 2012; published 7 June 2012)

Tachycardia and fibrillation are potentially fatal arrhythmias associated with the formation of rotating spiral waves in the heart. Presently, the termination of these types of arrhythmia is achieved by use of antitachycardia pacing or cardioversion. However, these techniques have serious drawbacks, in that they either have limited application or produce undesirable side effects. Low-energy far-field stimulation has recently been proposed as a superior therapy. This proposed therapeutic method would exploit the phenomenon in which the application of low-energy far-field shocks induces a large number of activation sites ("virtual electrodes") in tissue. It has been found that the formation of such sites can lead to the termination of undesired states in the heart and the restoration of normal beating. In this study we investigate a particular aspect of this method. Here we seek to determine how the activation site density depends on the applied electric field through *in vitro* experiments carried out on neonatal rat cardiac tissue cultures. The results indicate that the activation site density increases exponentially as a function of the intracellular conductivity and the level of cell isotropy. Additionally, we report numerical results obtained from bidomain simulations of the Beeler-Reuter model that are quantitatively consistent with our experimental results. Also, we derive an intuitive analytical framework that describes the activation site density and provides useful information for determining the ratio of longitudinal to transverse conductivity in a cardiac tissue culture. The results obtained here should be useful in the development of an actual therapeutic method based on low-energy far-field pacing. In addition, they provide a deeper understanding of the intrinsic properties of cardiac cells.

DOI: 10.1103/PhysRevE.85.061906 PACS number(s): 87.18.Hf, 05.45.−a, 87.19.Hh

I. INTRODUCTION

Undesired states in the heart, such as ventricular tachycardia (VT) and ventricular fibrillation (VF), can be life threatening. Developing a safe, reliable method for restoring normal rhythm to a heart is an important problem in modern medical science. Current treatments include antitachycardia pacing and cardioversion, but these techniques have serious drawbacks, in that they either have limited application or produce undesirable side effects, such as tissue damage and pain [1].

Recent studies have shown that low-energy far-field stimulation pacing (FFP) can also be used to reestablish the desired state in a heart. Furthermore, methodologies employing FFP do not have the limitations and side effects of current methodologies [1–4]. FFP techniques are known by various names, which all refer to essentially the same methodology: far-field antifibrillation pacing [1], wave emission from heterogeneities [2,5], application of virtual electrodes [6–8] and secondary sources to terminate arrhythmias [9], and low-energy antifibrillation pacing (LEAP) [4]. Although several studies have yielded results that have brought us closer to the clinical application of FFP, much remains to be understood [1,4,10–12].

Various underlying mechanisms and effects involved in FFP have been identified over the past decade. We now give a brief summary of the most important of these. One of the early studies that describes the effect of low-energy far-field shocks focuses on elucidating the existence and influence of anatomic heterogeneities that cause a polarization-depolarization distribution throughout the tissue [13]. Zemlin *et al.* [11] found that during near-threshold diastolic field stimulation, early activation occurs not only at the cathodal surface, as had been widely believed, but also deep inside the myocardium. Subsequent studies revealed that physical heterogeneities, such as scars and blood vesicles, can act as sources of secondary wave emission and can even be utilized in treatment for the termination of fibrillation-like states [2]. Early attempts to elucidate the potential application of FFP in low-energy defibrillation treatments were carried out through numerical bidomain studies. These studies indicated that FFP can be used to terminate spiral waves anchored to macroscopic obstacles [12,14] and that they might be even more efficient than high-frequency wave trains [3]. Applying the same scheme in *in vitro* experiments on cardiac tissue cultures, Cysyk and Tung [10] presented a possible strategy for terminating spiral waves anchored on millimeter-sized obstacles. Although it has been found theoretically that the phase of a spiral wave with respect to the applied electrical shock plays an important role [12,14], no clear dependence of this kind has been observed experimentally [10]. Also, although it has been predicted that the magnitude of the electric field required to induce wave propagation from obstacles increases as the size of the obstacle decreases [2], this too lacks experimental verification. In a recent study we showed that the minimum electric field necessary to induce waves from macroscopic obstacles is modulated by local tissue heterogeneities [5]. This study thus showed that the situation *in vivo* is much different from that *in vitro*. It has been shown that such conductivity gaps

*Corresponding author: marcel@cdb.riken.jp

and conductivity discontinuities are effective for generating activation sites and also create activation delays that depend on the electric field strength [1,4]. Luther *et al*. showed using a canine wedge preparation consisting of a right atrium and right ventricle that as the electric field strength increases, the number of sources increases over the entire tissue sample and that the activation time decreases. There it is conjectured that the wave sources originate from different heterogeneities in the tissue, such as blood vessels, boundaries between regions of different fiber alignment directions, fatty tissue, and intercellular clefts [4]. Such activation sites can be used to terminate obstacle-anchored spiral waves (anatomical reentries), which tend to become pinned on heterogeneities [15], as has been shown both theoretically [12,16] and experimentally [10,17]. Furthermore, it has been found that FFP is even capable of terminating arrhythmia in atrial tissue [1].

In this study we examine the effect of conductivity discontinuities in detail. We focus on the dependence on the applied electric field and conductivity distribution, assuming that local conductivity discontinuities are sufficient to produce activation sites. Employing numerical bidomain simulations and experiments on cardiac tissue cultures, we find that the activation site density (ASD) increases exponentially as a function of the electric field. We also derive an intuitive theoretical framework that shows that the minimum electric field needed to obtain activation sites depends mainly on the intracellular conductivity and the level of cell isotropy. Furthermore, we determine the ratio of transverse to longitudinal intracellular conductivity in a cardiac tissue culture.

II. MATERIALS AND METHODS

Experiments were performed on cardiac tissue cultures. Simulations employing the Beeler-Reuter (BR) model [18,19], a Hodgkin-Huxley-type ionic current model of the mammalian ventricular myocardial cell [20,21], were adapted using controllable cell-distribution functions in order to obtain a qualitative description and used as a foundation for deriving an analytical framework.

A. Experimental methods

Cell culture. The protocol used for a primary cardiomyocyte culture has been documented previously [22,23]. Briefly, hearts isolated from neonatal 2-day-old Wistar rats were minced and digested enzymatically using collagenase. The isolated cells were collected by centrifugation and preplated for 1 h. After the supernatant was collected again, the cells were plated on 22-mm-diameter glass coverslips coated with fibronectin 12 g/ml at a cell density of 2.63×10^3 cells/mm^2. Cell constructs were incubated in Dulbecco-modified Eagle Medium with 10% fetal bovine serum and 1% penicillin streptomycin for 24 h under humidified conditions at 37 °C and 5% CO_2. The medium was then replaced with a contraction medium, Minimum Essential Medium, with 10% calf serum, 1% penicillin streptomycin, and Cytosine Arabino-Furanoside (ARA-C), a proliferation inhibitor, to minimize the number of fibroblasts [24,25]. The last step was omitted in some parts of the study in order to clarify the role of fibroblasts. Experiments on 30 independent cardiac tissue cultures are performed utilizing 17 layers with ARA-C and 13 layers without ARA-C.

Observations. Experiments were performed 4 days after plating. Before each observation, cells were labeled with the Ca^{2+}-sensitive fluorescent dye Fluo-8, and the medium was replaced with Tyrode solution at room temperature. Fluorescence was observed using an inverted microscope (IX-70; Olympus, Tokyo Japan) with a ×2.0 magnification objective lens (PLAPON, N.A. = 0.08, Olympus) in combination with a ×0.35 intermediate lens [26] to count activation sites. Raw images were obtained with an electron-multiplying CCD camera (iXon DV887ECS-UVB; Andor) with 64×64 pixels at a 14-bit resolution with 200 frames/s after 8×8 binning. High-magnification pictures were obtained by confocal laser scanning fluorescence microscopy (Carl Zeiss LSM510) using ×20 and ×40 magnification objective lenses.

Electrical stimulation. Far-field stimulation was applied with 10-ms bipolar pulses delivered through 3.5-cm-spaced platinum electrodes on either edge of the sample. The electric field was varied systematically in the range 1.0 to 2.5 V/cm in steps of 50 mV/cm. Three stimuli were applied with a frequency of 1 Hz. Activation sites were counted only when observed in all three responses, to exclude the possibility of mistakenly counting spontaneous calcium releases.

Data analysis. Data were processed using ImageJ [27] analysis software with custom plug-ins. The time series for each pixel were filtered using a Savitzky-Golay filter for noise reduction.

Ethics statement. This study was carried out in strict accordance with the guidelines for animal experimentation established by the Animal Research Committee, Kyoto University. The protocol was approved by the Animal Research Committee, Kyoto University (Permit Number H22023).

B. Numerical methods

We performed numerical simulations of the cardiac equations, using the BR model [18]. Integration methods employed in numerical studies of the bidomain model are discussed by Keener and Bogar [29]; we used the Crank-Nicolson method. The intracellular and extracellular membrane potentials Ψ_i and Ψ_e, respectively, satisfy the relations

$$\nabla \cdot (\hat{\sigma}_i \nabla \Psi_i) = +\beta \left[C_m \frac{\partial}{\partial t} (\Psi_i - \Psi_e) + I_{\text{ion}} \right] + J_i \qquad (1)$$

and

$$\nabla \cdot (\hat{\sigma}_e \nabla \Psi_e) = -\beta \left[C_m \frac{\partial}{\partial t} (\Psi_i - \Psi_e) + I_{\text{ion}} \right] + J_e, \qquad (2)$$

where $\hat{\sigma}_i$ and $\hat{\sigma}_e$ are the conductivity tensors, C_m is the membrane capacitance per unit area of the cell membrane, β is the ratio of the membrane surface area to the tissue volume, and J_i and J_e are the currents per unit volume. The latter are obtained by scaling from the externally injected currents I_i and I_e in the intracellular and extracellular spaces on the boundary of the system. These are given by

$$I_{i,e} = \bar{\boldsymbol{n}} \cdot \hat{\sigma}_{i,e} \boldsymbol{E} = -\bar{\boldsymbol{n}} \cdot \hat{\sigma}_{i,e} \nabla \Psi_{i,e}, \qquad (3)$$

where E is the externally applied electric field, and $\bar{n}$ is the unit vector normal to the boundary. Equation (3) implies Neumann

boundary conditions in the case that $E = 0$. Four different currents are considered in the model: the time independent and time dependent slow outward currents of potassium, the fast inward current of sodium, and the slow inward current of calcium. The maximum conductance for the last of these is set to $g_{Ca} = 0.045$ mS/cm^{-2} [12,14]. These currents are controlled by six gating variables (x_1, m, h, j, d, f), which all obey the same type of ordinary differential equation. Explicitly, that for m is

$$\frac{dm}{dt} = \frac{\bar{m}(\Psi) - m}{\tau_m(\Psi)}, \tag{4}$$

where the fast gating variable m is treated adiabatically at each time step as $\bar{m}(\Psi) = m(t)$ to optimize the integration protocol, as described previously [5,14,19].

The extracellular conductivity was chosen to be isotropic, that is, $\sigma_{e,\perp} = \sigma_{e,\parallel}$, as in the presently investigated experimental system, and the intracellular longitudinal conductivity $\sigma_{i,\parallel}$ was assumed to be equal to the extracellular conductivity [30–32]. Simulations were performed with spatial and temporal step sizes of 0.015 cm and 0.05 ms, with a grid size of 200 × 200 units, corresponding to an effective tissue area of 9 cm^2. The spatiotemporal resolution was chosen to sufficiently resolve the behavior of the system (see Fig. 1). The local variation in the cell orientation of the tissue was adjusted by defining the alignment angle randomly for each cell. Explicitly, writing

$$\Delta\Phi = \Phi_{\max} - \Phi_{\min}, \tag{5}$$

we fixed $\Phi_{\min} = 0$ and varied $\Phi_{\max}$ between 0.05π and 0.5π, which correspond to almost complete cell alignment and full cell isotropy, respectively. In the latter case, cells have no preferred alignment, and thus, the distribution of angles is normal. The intracellular conductivities are expressed by the following elliptical equations:

$$\sigma_{i,x} = \frac{\sigma_{i,\perp}\sigma_{i,\parallel}}{\sqrt{\sigma_{i,\parallel}^2 \cos^2(-\omega_{xy}) + \sigma_{i,\perp}^2 \sin^2(-\omega_{xy})}}, \tag{6}$$

$$\sigma_{i,y} = \frac{\sigma_{i,\perp}\sigma_{i,\parallel}}{\sqrt{\sigma_{i,\parallel}^2 \cos^2\left(\frac{\pi}{2} - \omega_{xy}\right) + \sigma_{i,\perp}^2 \sin^2\left(\frac{\pi}{2} - \omega_{xy}\right)}}. \tag{7}$$

Here $\sigma_{i,x}$ and $\sigma_{i,y}$ are the projected conductivities induced parallel and perpendicular to the electric field, respectively, and ω_{xy} is the angle of cell alignment, defined as

$$\omega_{xy} = N\Delta\Phi - \Phi_{\min}, \tag{8}$$

where N is the uniform distribution function, which is between 0 and 1. The longitudinal and transverse intracellular conductivities were chosen to be 0.4 and 0.1 S m^{-1} for one set and 0.2 and 0.02 S m^{-1} for the other. The value of $\Phi_{\max}$ was varied between 0.05π and 0.5π, while $\Phi_{\min}$ was fixed at 0.0π. Therefore, by definition, the direction of the applied electric field approached the direction of the longitudinal intracellular conductivities as $\Phi_{\max}$ decreased. Intracellular conductivity values were chosen in the range [0.2,0.5] S m^{-1} for $\sigma_{i,\parallel}$ and [0.04,0.10] S m^{-1} for $\sigma_{i,\perp}$, considering full isotropy ($\Phi_{\max} = 0.5$).

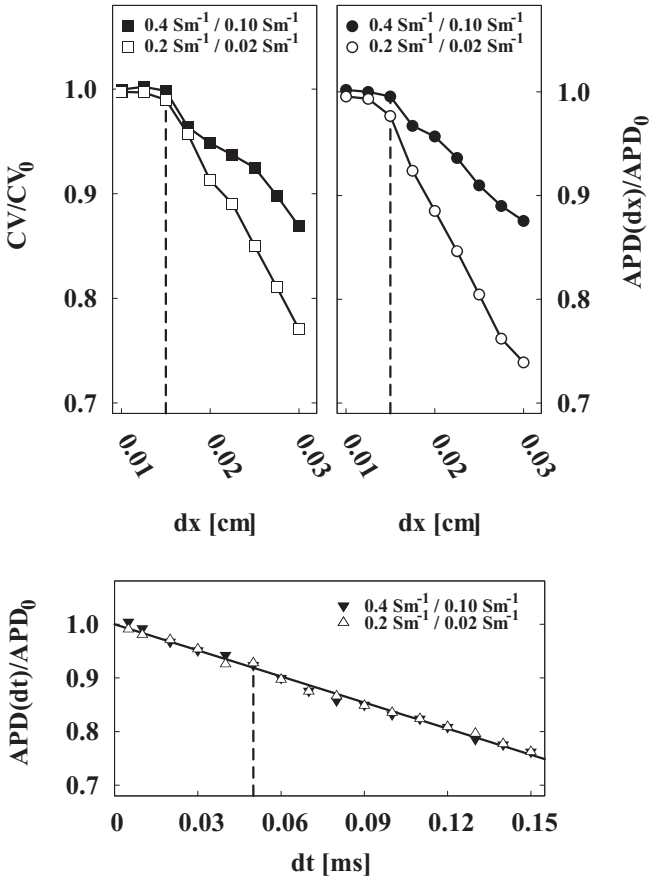

FIG. 1. Dependence of the conduction velocity (CV) and action potential duration (APD) on the spatial and temporal resolution for the Beeler-Reuter model using the Crank-Nicolson method for two sets of conductivities, 0.4 and 0.1 S m^{-1} (shaded symbols) and 0.2 and 0.02 S m^{-1} (undashed symbols). As shown by Clayton *et al.*, the CV is more sensitive to the spatial resolution than the APD [28]. The black dashed lines correspond to the spatial and temporal step sizes used in this study ($dx = 0.015$ cm; $dt = 0.05$ ms). This temporal resolution results in an error in the APD of approximately 8%, as determined by the value of the APD, in the $dt \to 0$ limit. APD_0 and CV_0 are the estimated values of the APD and CV in the $dt \to 0$ and $dx \to 0$ limits.

III. RESULTS

A. Experiments on cardiac tissue

We sought to quantify the dependence of the number of activation sites on the electric field strength in application of FFP. For this purpose we investigated an *in vitro* experimental system consisting of a cardiac tissue culture that exhibits natural cell isotropy. Thus, in this sample there existed conductivity discontinuities distributed over virtually all of the tissue. Seventeen tissue cultures were observed, as described above (see Sec. II). The observed activation sites were counted, and the resulting number was divided by the area of the field of observation to obtain the ASD. Activation sites were distinguished at a minimum distance of ∼0.5 mm, which is on the order of the dimension of the liminal area of the tissue. Furthermore, the time delay of the depolarization of the activation sites was considered within a time window of 20 ms, which corresponds to four recorded frames [1]. Figure 2(a)

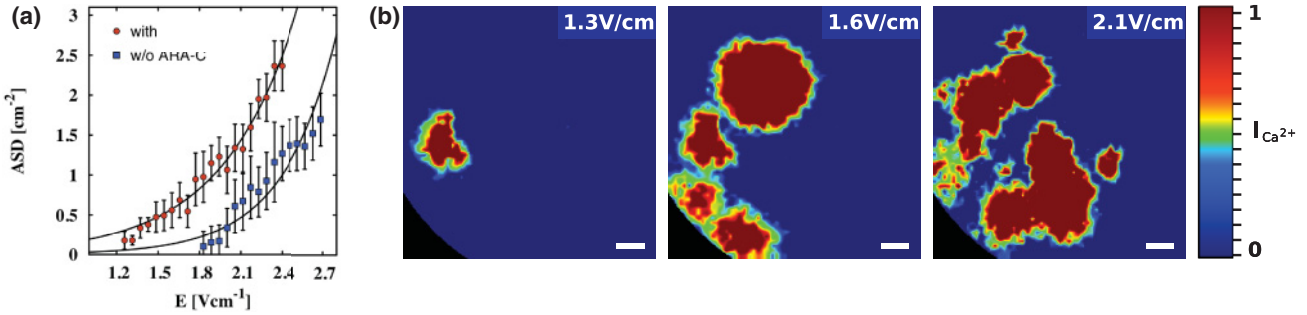

FIG. 2. (Color online) Experimental results for the activation site density (ASD) in a cardiac tissue culture. (a) Data depicting the increase in the ASD as a function of the applied electrical field, represented by the red circles and blue squares, for the experiments performed with and without the proliferation inhibitor ARA-C, respectively. The black error bars indicate the standard deviations (half-width) of the ASD. The black solid curves represent the fit provided by Eq. (15). (b) Snapshots of initiated activation sites in the same sample for three values of the applied electric field in culture with ARA-C. These images were taken 10 ms after the shock was applied. The color indicates the normalized calcium intensity. The green (bright) area corresponds to the wavefront of the target waves, and the black area in the lower left corner corresponds to the boundary of the tissue. The white bars represent a length of 0.1 cm.

displays the ASD plotted as a function of the applied electric field strength in cardiac tissue culture. The red circles and blue squares are the experimental data points for cultures with and without ARA-C, respectively, and the black solid curves represent the best fitting exponential forms. Figure 2(b) displays snapshots of activation site distributions for applied electric field strengths of 1.3, 1.6, and 2.1 V/cm, respectively. Wavefronts appear in green (bright), and the red and blue areas correspond to excited and unexcited tissue, respectively.

Figure 3 displays fluorescence images (upper rows) and phase contrast images (lower rows) of the cardiac tissue culture with and without the proliferation inhibitor ARA-C, respectively. The black areas correspond to fibroblasts or, possibly, regions that lack cells. ARA-C inhibits the production (cell division) of fibroblasts, which are nonexcitable cells that maintain the structural integrity of tissue, and thus act as purely diffusive media. Additionally, two important properties of fibroblasts are their motility, that is, their ability to exhibit spontaneous motion, and their formation of clusters during the developmental stage of the tissue [33,34]. In *in vitro* engineered cardiac tissue cultures, cells are generally distributed isotropically. However, we found that the presence of fibroblasts increases the value of the minimum electric field strength necessary to produce activation sites. This can be understood from the increase in the liminal area and liminal current (minimum area and current that define the excitation threshold of a propagating target wave) necessary to observe excitation of activation sites [35,36]. It is also reflected by the slowing in the rate at which the conductivity decreases, as observed by Zlochiver *et al.* [37], which may be caused by a change in the cell physiological parameters, as indicated by the change in cell size (see Fig. 3). A further (at this point quite hypothetical) possible effect is the influence of motile fibroblasts on cardiac tissue during the developmental stage of the tissue resulting from the contraction-induced cluster formation of fibroblasts [33,34]. This could lead not only to a change in cell morphology but also to a change in local cardiac cell alignment.

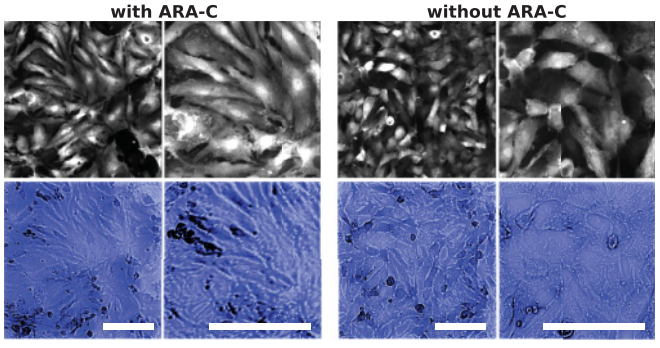

FIG. 3. (Color online) Isotropically distributed cell culture in cases with and without ARA-C. The upper left and right rows display images of the cardiac tissue culture at two different scales for systems cultured with and without the proliferation inhibitor ARA-C, respectively. The brightness level indicates the free calcium-ion concentration in cardiac cells. The blue images (lower rows) are the phase-contrast snapshots corresponding to the upper figures. The white bars represent a length of to 100 μm.

B. Numerical simulations

We performed numerical simulations of cardiac tissue using the BR model to help interpret our experimental results (see Sec. II). Longitudinal and transverse intracellular conductivities were chosen arbitrarily to be 0.4 and 0.1 S m^{-1} for the first set and 0.2 and 0.02 S m^{-1} for the second. Cells were randomly distributed in accordance with Eq. (6) by varying the maximum alignment opening angle of the cell distribution $\Delta\Phi$ [see Eq. (5)], from isotropic 0.5π, to almost perfectly aligned 0.05π. Figure 4(b) contains snapshots of activation site distributions ($\Delta\Phi = 0.5\pi$) at applied electric fields of 5.3, 5.7, and 6.3 V/cm, respectively. As in the experimentally obtained snapshots [see Fig. 2(b)], wavefronts appear in green, and the red and blue areas correspond to excited and unexcited tissue, respectively. The ASD for this numerical system was determined similarly to that for the experimental system. First, activation sites were counted. We included sites that appeared as long as ~50 ms after the application of the electric field [1]. Then we divided the number of sites by the area of the system to obtain the ASD. The planar wave that emanated from the right boundary was not taken into account, because

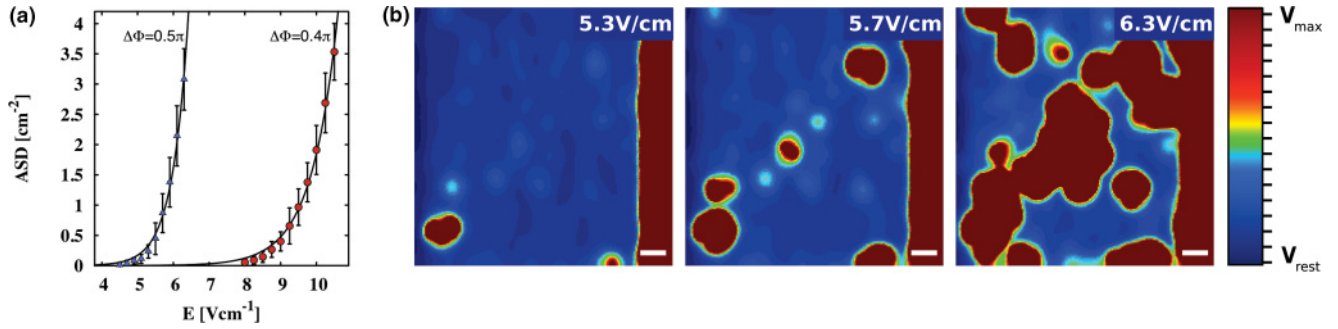

FIG. 4. (Color online) Results of numerical simulations for the activation site density (ASD). (a) The value of the ASD as a function of the electric field strength for $\sigma_{e,\parallel} = \sigma_{e,\perp} = \sigma_{i,\parallel} = 0.4$ S m^{-1} and $\sigma_{i,\perp} = 0.1$ S m^{-1}. The triangles and circles are the results for the cases in which the maximum alignment opening angle of the cell distribution $\Delta\Phi$ is 0.5π and 0.4π, respectively. The black error bars represent the standard deviations of the results obtained from 10 numerical simulations for each value of $\Delta\Phi$, and the black solid curve is the fit provided by the derived equation, Eq. (15). b) Snapshots of target waves produced with three different electric field strengths in the case $\Delta\Phi = 0.5\pi$. These snapshots were taken 16 ms after the shock was applied. The green (bright) intensity level corresponds to the wavefront of the target waves. The white bars represent a length of 0.3 cm.

it was not caused by tissue heterogeneity. Figure 4(a) plots the obtained ASDs as a function of the electric field strength for $\Delta\Phi = 0.5\pi$ and $\Delta\Phi = 0.4\pi$ with the blue triangles and red circles, respectively. We find that as the local variation of cell orientation increases ($\Delta\Phi \to 0$), the magnitude of the electric field required to induce activation sites in the medium increases, while the slope of the ASD curve as a function of the electric field decreases.

C. Theoretical investigation

To obtain an analytical description of both our experimental observations and our numerical results, we now derive an intuitive analytical framework. We study the bidomain equations (1) and (2), and consider the case in which the membrane potentials Ψ_i and Ψ_e are constant in time. From these, we derive an expression representing an exponential dependence of the number of activation sites on the magnitude of the applied electric field. Next, we derive an expression for the membrane potential as a function of the intracellular conductivity distribution in cardiac cells. This allows us to extract information regarding the intracellular conductivity ratio from the experimental data.

We begin by considering the case of a fixed membrane potential distribution with a uniformly applied current density I_e, which is applied at the edge of the system by electrodes. For weak electric fields, Eqs. (1) and (2) can be linearized in terms of the membrane potential $V_m = \Psi_i - \Psi_e$ and $I_{\text{ion}} = G_m V_m$ as follows:

$$\nabla \cdot (\hat{\sigma}_e \nabla \Psi_e) = -\beta G_m V_m - I_e, \tag{9}$$

$$\nabla \cdot [(\hat{\sigma}_e + \hat{\sigma}_i)\nabla \Psi_e + \hat{\sigma}_i \nabla V_m] = 0, \tag{10}$$

where $\beta = 2000$ cm^{-1} and $G_m = 0.165$ mS/cm^2 [12,14]. Thus, if we assume that the inward flux is perpendicular to the electric field due to induced conductivity heterogeneities, and that the inward and outward flux on the cell membrane is conserved, Eq. (9) can be rewritten as

$$-\hat{\sigma}_e E_0(\Delta\Phi) = -\frac{1}{d}\oint_s (\beta G_m V_m + I_e)\, dA, \tag{11}$$

where E_0 is the minimum electric field needed to obtain activation sites in the medium for a given angle distribution $\Delta\Phi$, and d is the distance between the parallel electrodes, which is set to 3.5 and 3 cm in the experiments and numerical simulations, respectively. Without loss of generality, we can solve the above integral considering A to be $A_0 = 1$ cm^2. We then obtain

$$I_e A_0 d^{-1} - \hat{\sigma}_e E_0(\Delta\Phi) = -\beta G_m V_m A_0 d^{-1}. \tag{12}$$

Next, we redefine the extracellular conductivity tensor $\hat{\sigma}_e$ to be a constant scalar, because we assume that the extracellular conductivity is isotropic ($\sigma_{e,\parallel} \equiv \sigma_{e,\perp}$) and that $\sigma_{e,\parallel}/\sigma_{i,\parallel} = 1$. Both of these assumptions are supported by experiments conducted with Tyrode solution on cardiac tissue cultures (see Sec. II) [30–32]. We make the same assumptions for the numerical simulation (see Sec. II).

With the above assumptions, we can write Eq. (12) in the more general form

$$\sigma_e\left(\frac{A_0 I_e}{\sigma_e d} - E_0\right) = -\beta G_m V_m A_0 d^{-1}, \tag{13}$$

where we define the applied electric field as

$$E = \frac{A_0 I_e}{\sigma_e d}. \tag{14}$$

Finally, we assume that the ASD is an exponential function of E, as observed experimentally [Fig. 4(a)], and we assume that it takes the form

$$\rho_{\text{ASD}} \propto \rho_0 \exp\left(\frac{E - E_0(\Delta\Phi)}{\kappa}\right), \tag{15}$$

where ρ_0 is set to unity (1 cm^{-2}), and κ is defined as

$$\kappa^{-1} = \frac{\sigma_e}{\beta G_m V_m(\Delta\Phi) A_0 d^{-1}}. \tag{16}$$

We fit Eq. (15) as a function of the electric field E to the numerical results (black curves in Fig. 4) and thereby obtained the values of E_0 and σ_e/V_m, which depend on the

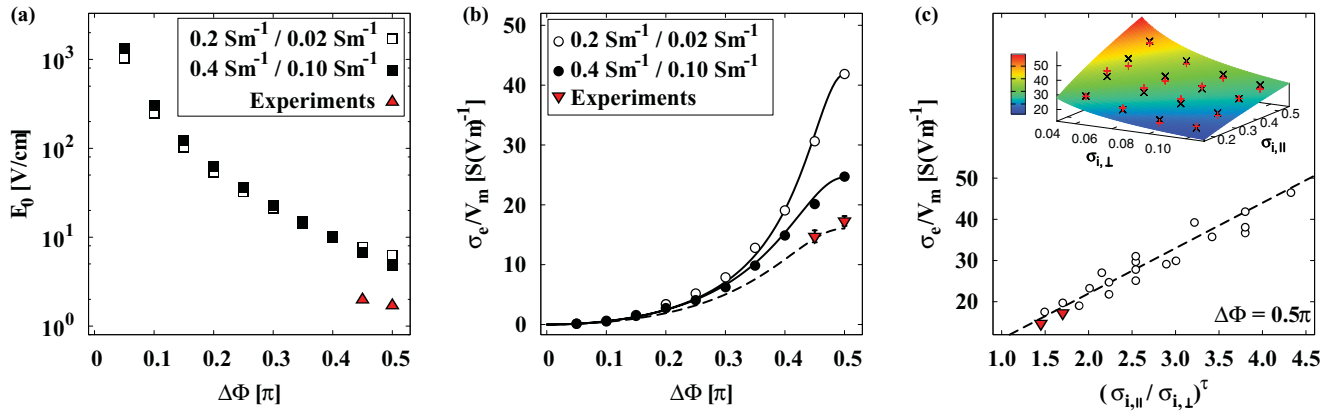

FIG. 5. (Color online) Results for E_0 and the effective conductivity. (a) The minimum electric field necessary to produce activation sites E_0. (b) The ratio of the extracellular effective conductivity σ_e to the membrane potential V_m as a function of the maximum alignment opening angle $\Delta\Phi$. The shaded symbols represent the values obtained from numerical simulations with $\sigma_{e,\parallel} = \sigma_{e,\perp} = \sigma_{i,\parallel} = 0.4$ S m^{-1} and $\sigma_{i,\perp} = 0.1$ S m^{-1}, and the unshaded symbols represent those obtained with $\sigma_{e,\parallel} = \sigma_{e,\perp} = \sigma_{i,\parallel} = 0.2$ S m^{-1} and $\sigma_{i,\perp} = 0.02$ S m^{-1}, respectively. The upwardly and downwardly directed triangles represent the experimentally obtained values of E_0 and σ_e/V_m, respectively. The quantity σ_e/V_m is obtained as 17.31 ± 0.82 and 10.04 ± 1.64 S(V m)$^{-1}$ for cultures with and without ARA-C, respectively. The latter is assumed to be $\Delta\Phi = 0.45\pi$ to investigate the validity of the working hypothesis that the existence of fibroblasts leads to an increase of the anisotropy. The black solid curves represent the theoretical prediction obtained from Eq. (17), and the black dashed curve represents the best fit provided by Eq. (17) to the experimental data. (c) Dependence of σ_e/V_m on $\alpha \equiv (\sigma_{i,\parallel}/\sigma_{i,\perp})^\tau$ with $\tau = 0.58$ as found numerically (circles) and experimentally (triangles). The inset shows how σ_e/V_m with $\Delta\Phi = 0.5\pi$ depends on $\sigma_{i,\perp}$ and $\sigma_{i,\parallel}$. The analytic prediction for σ_e/V_m [see the black dashed curve in panel (b) and Eq. (17)] is represented by the surface. The X symbols and the plus signs are the analytic and numerical results, respectively.

local variation in the cell orientation $\Delta\Phi$. In the fitting, the parameters β, G_m, A_0, and d were assumed to be fixed to the values introduced in the previous section. Figure 5(a) displays E_0 as a function of $\Delta\Phi$ (squares) and the ratio of σ_e to V_m circles for two sets of values of the conductivities for which the ratios of the transverse to longitudinal conductivities are 4 and 10, respectively.

Henceforth, we focus only on the ratio of σ_e to V_m, because we are interested in the relationship between V_m and the intracellular conductivity of the cardiac cells. For our analytic description, we assume that a wave originates if the ionic transport between the intracellular and extracellular regions is sufficiently strong and if the local excitation induced by the outward flux of electrons (inward flux of Na^+) caused by the electric field is sufficient to lead to wave propagation [2,5]. To satisfy both of these conditions, the respective resistances must be overcome. Thus, we can approximate σ_e/V_m by the elliptical relationship

$$\frac{\sigma_e}{V_m} \sim \frac{\alpha\gamma}{\sqrt{\alpha^2\cos^2(\Delta\Phi) + \gamma^2\sin^2(\Delta\Phi)}}, \tag{17}$$

with the parameters

$$\alpha = \left(\frac{\sigma_{i,\parallel}}{\sigma_{i,\perp}}\right)^\tau + \gamma \tag{18}$$

and

$$\gamma = 1, \tag{19}$$

where α defines the projected conductivity, assuming an elliptic conductivity tensor with $\sigma_{i,\parallel}$ and $\sigma_{i,\perp}$, and $\tau = 0.58$ is a free parameter that has been determined so as to best fit the numerical and experimental data. Here we point out that γ may depend on the extracellular conductivities; that is, it may be a function of σ_e. However, the choice $\sigma_{e,\parallel} = \sigma_{e,\perp} = \sigma_{i,\parallel}$ made in order to allow comparison with the experimental results leads to the simple relation given in Eq. (19). The dependence of σ_e/V_m on $\Delta\Phi$ is plotted in Fig. 5(b) with the black solid curves. The respective slopes of Eq. (17) are consistent with the numerical results. The triangles indicate the obtained ratios of σ_e/V_m from the experimental data in the cases with and without ARA-C at $\Delta\Phi = 0.50\pi$ and $\Delta\Phi = 0.45\pi$, respectively. The black dashed curve is that obtained using the value of α that yields the best fit, which corresponds to an intracellular conductivity ratio of $\sigma_{i,\parallel}^{\rm exp}/\sigma_{i,\perp}^{\rm exp} = 2.5 \pm 0.2$. Here we assumed that the existence of fibroblasts, which are observed in experiments without ARA-C, leads to an increase in the cellular anisotropy. This assumption can be reasoned by the contraction-induced cluster formation of fibroblasts during the developmental stage of the tissue [33,34]. Based on our knowledge of the slope (represented by the black dashed curves), we deduce the relation $\Delta\Phi \approx 0.45\pi$ for the angle distribution of the experimentally investigated cardiac tissue without ARA-C. Without discussing the cause of the difference in membrane potential (ratio of σ_e and V_m) that we obtained through the theoretical approximation, we estimate an effective change of approximately 10 deg in the angle distribution. The red triangles in Fig. 5(a) indicate the respective electric fields $E_0^{\rm exp}$. The experimental data corresponding to 0.5π and 0.45π are presented in Fig. 2(a) with red circles (with ARA-C) and blue squares (without ARA-C), respectively. Table I gives an overview of the intracellular conductivities and the respective ratios found in previous studies on mammalian cardiac cells and, for comparison, the ratio determined using the cardiac tissue culture.

We performed further numerical simulations in which we varied the cell conductivities of isotropically distributed cell

TABLE I. Conductivity values (S/m) obtained from *in vivo* experiments on cardiac tissue reported in the literature and estimated intracellular conductivity ratios obtained in the present study examining *in vitro* cardiac tissue cultures.

References	$\sigma_{i,\parallel}$	$\sigma_{i,\perp}$	$\sigma_{i,\parallel}/\sigma_{i,\perp}$
Clerc (1979) [38]	0.17	0.019	8.95
Roberts *et al*. (1979) [39]	0.28	0.026	10.77
Roberts *et al*. (1982) [40]	0.34	0.06	5.67
LeGuyader *et al*. (1995) [41]	0.20	0.024	8.33
Stinstra *et al*. (2005) [42][a]	0.16	0.005	32.0
Fishler (1998) [13][a]	0.17	0.01	17.0
Present study examining on *in vitro* cardiac tissue culture:			
with ARA-C			2.5 ± 0.2
w/o ARA-C			1.9 ± 0.2

[a]Data obtained from numerical model.

media ($\Delta\Phi = 0.5\pi$), and determined σ_e/V_m by using Eq. (15). The circles in Fig. 5(c) plot the obtained ratios of σ_e/V_m as a function of α [see Eq. (17)]. The black dashed line corresponds to the case in which α with $\tau = 0.58$, which yields the best fit to the obtained data points. The triangles indicate the experimentally obtained values of $\sigma_e^{\exp}/V_m^{\exp}$. Anisotropy ratios of 2.5 and 1.9 were found in cardiac tissue with and without ARA-C, with fully isotropic cell distributions ($\Delta\Phi = 0.5\pi$) for both cultures. Here fibroblasts are interpreted as purely diffusive media (nonexcitable) that have no direct influence on the excitation. However, their presence increases the liminal area of excitation that yields wave propagation, because their existence causes the ratio of conducting cells to nonconducting cells to decrease. The inset of Fig. 5(c) plots the ratio that depends on the intracellular conductivity for $\sigma_{i,\parallel} \in [0.2,0.5]$ S m^{-1} and $\sigma_{i,\perp} \in [0.04,0.10]$ S m^{-1} with the plus signs. The X symbols represent the corresponding ratio of σ_e to V_m for the analytic prediction represented by the surface.

The mechanisms that underlie the analytical description can be summarized as follows. The product of the electric field strength and the ratio of extracellular conductivity to the membrane potential can be considered constant, as defined by the local current density, because it depends only on system constants. Explicitly, from Eq. (13) we have

$$E\frac{\sigma_e}{V_m} \sim -\beta G_m A_0 d^{-1}. \tag{20}$$

Thus, the membrane potential regulates the electric field strength required to obtain wave propagation. Because we do not have reliable values of β and G_m for our experimental setup, we compare the ratio of E to κ, which is proportional to the externally applied current density I_e [see Eqs. (14) and (16)]. For $E\kappa^{-1}$ we obtained the values 13.0 ± 1.0 and 17.3 ± 1.2 for the two considered sets of conductivities, $\sigma_{e,\parallel} = \sigma_{e,\perp} = \sigma_{i,\parallel} = 0.4$ S m^{-1} and $\sigma_{e,\parallel} = \sigma_{e,\perp} = \sigma_{i,\parallel} = 0.2$ S m^{-1} (see Fig. 5), respectively. The experimental data yield $E\kappa^{-1} = 3.09 \pm 0.02$, which implies that the value of βG_m used in the numerical simulations is larger than the actual value in the experimental system.

IV. CONCLUSION

We studied the ASD, which is a function of the applied low-energy far-field stimulation field strength, both numerically and experimentally. We found that the ASD increases exponentially as a function of the electric field strength. We also found that the minimum value of the electric field strength necessary to observe activation sites increases as a function of the angle distribution of cells in the medium, which defines the level of isotropy. We derived an intuitive theoretical framework that qualitatively describes the ASD in terms of an effective conductivity. Furthermore, we found using Eq. (17) that the ratio of the intracellular transverse conductivity to the longitudinal conductivity was approximately 2.5 and 1.9 in the experimental *in vitro* cultured cardiac tissue in the cases with and without ARA-C, respectively (see Fig. 3 for comparison). These values are approximately 3 to 4 times smaller than the intracellular conductivity ratios obtained experimentally in *in vivo* studies, for which there was natural cell alignment (see Table I). The intracellular conductivity ratios listed for comparison in Table I were obtained with various methods using *in vivo* heart preparations of different types, such as trabecular bundles from the right ventricle of calf hearts, mongrel dogs, and canine left ventricular myocardia, respectively [38–40]. All of these values were obtained through comparison of the conduction velocities of longitudinal and transverse propagating waves in the tissue.

The difference between the values obtained from the numerical and experimental data suggests that the details of the electrical dynamics of the Beeler-Reuter model differ from those exhibited by the experimental system consisting of the cardiac tissue of a neonatal rat. The membrane potential can be expressed as a function of the intracellular conductivities taking the form of an elliptic euqtion [see Eq. (17)], which is characterized by two thresholds. First, the ratio of the intracellular transverse and longitudinal conductivities defines the threshold of wave propagation in the medium. Second, the intracellular transverse conductivity defines the threshold of transmembrane conduction. Here it is important to note that the assumed conductivity relation ($\sigma_{e,\perp} = \sigma_{e,\parallel} = \sigma_{i,\parallel}$) is based on previous findings for *in vitro* experiments carried out on a cardiac tissue culture using Tyrode solution as a buffer [30–32]. However, native cardiac tissue does not allow such an assumption. The conductivities are determined by the properties of the intracellular and extracellular tissue only.

Our results indicate that cell alignment in the tissue plays an essential role in the application of low-energy far-field pacing. However, several problems may arise in the attempt to extend our work to actual, intact hearts. In a real beating heart, cells are generally distributed anisotropically; however, scars and cancerous tissue might change the local variation in cell orientation and thus serve as primary activation sites when low-energy far-fields are applied. This would be disadvantageous, because induced reentries tend to anchor on such heterogeneities and can lead to stable arrhythmia or even fibrillation [15]. Furthermore, our results indicate that it might be possible to determine the intracellular cardiac conductivity when a tissue culture with different cell alignments is used. Studies employing hydrogen gel [43] and microelastic gelatinous gels [44] may be useful in this regard. Improving cardiac

conduction through use of patterned cell cultures on rigid gel substrates that mimic the extracellular environment is a possible topic for a future investigation. Such a study could be used to examine more closely native cell functionality and natural anisotropy in order to obtain more realistic and precise values of conductivity ratios of heart tissue [45]. Additionally, the choice of a more detailed electrophysiological model or a model more faithfully describing the neonatal rat cell electrophysiology [46] may yield results with greater accuracy. Our procedure for adiabatically eliminating the m gate may modify the model's conduction velocity, as has been shown previously [47]. Additional errors may result from limitations in accounting for the behavior of the system at the time of a shock [48,49] and the fact that our numerical results were obtained by examining the membrane potential, while our experimental results were obtained by observing the intracellular calcium.

Although our experimental and numerical results exhibit consistency, three-dimensional studies are necessary to provide a full picture of the application of low-energy far-field stimulation to the termination of arrhythmia, because additional effects, such as vesiculation, cell alignment distributions, and boundary effects of local heart compartments, may also play important roles, as suggested recently by Luther *et al*. [4].

This study not only furthers our understanding of the application of FFP to real beating hearts, but also suggests a way to gain insight into the intrinsic properties of cardiac cells. The determination of cardiac cell conductivity could be a future application of this approach.

ACKNOWLEDGMENTS

The authors thank Makito Miyazaki and Emilia Entcheva for their helpful discussions, and Glenn Paquette for use of the *DIVE* proofreading software. This work was supported by the Japan Science and Technology Agency, Core Research on Evolutional Science & Technology (CREST, Team Kageyama), and a Grant-in-Aid for Scientific Research (A) (No. 23240044) from the Japan Society for the Promotion of Science (JSPS).

[1] F. Fenton, S. Luther, E. Cherry, N. Otani, V. Krinsky, A. Pumir, E. Bodenschatz, and J. R. F. Gilmour, Circulation **120**, 467 (2009).
[2] A. Pumir, V. Nikolski, M. Hörning, A. Isomura, K. Agladze, K. Yoshikawa, R. Gilmour, E. Bodenschatz, and V. Krinsky, Phys. Rev. Lett. **99**, 208101 (2007).
[3] P. Bittihn, G. Luther, E. Bodenschatz, V. Krinsky, U. Parlitz, and S. Luther, New J. Phys. **10**, 103012 (2008).
[4] S. Luther, F. Fenton, B. Kornreich, A. Squires, P. Bittihn, D. Hornung, M. Zabel, J. Flanders, A. Gladuli, L. Campoy *et al*., Nature (London) **475**, 235 (2011).
[5] M. Hörning, S. Takagi, and K. Yoshikawa, Phys. Rev. E **82**, 021926 (2010).
[6] E. Sobie, R. Susil, and L. Tung, Biophys. J. **73**, 1410 (1997).
[7] E. Entcheva, J. Eason, I. Efimov, Y. Cheng, R. Malkin, and F. Claydon, Cardiovasc. Electrophysiol. **9**, 949 (1998).
[8] I. Efimov, F. Aguel, Y. Cheng, B. Wollenzier, and N. Trayanova, Am. J. Phys. Heart Circ. Physiol. **279**, H1055 (2000).
[9] V. Fast, S. Rohr, A. Gillis, and A. Kleber, Circ. Res. **82**, 375 (1998).
[10] J. Cysyk and L. Tung, Biophys. J. **94**, 1533 (2008).
[11] C. Zemlin, S. Mironov, and A. Pertsov, Cardiovasc. Res. **69**, 98 (2006).
[12] S. Takagi, A. Pumir, D. Pazo, I. Efimov, V. Nikolski, and V. Krinsky, Phys. Rev. Lett. **93**, 058101 (2004).
[13] M. Fishler, J. Cardiovasc. Electrophysiol. **9**, 384 (1998).
[14] S. Takagi, A. Pumir, D. Pazo, I. Efimov, V. Nikolski, and V. Krinsky, J. Theor. Biol. **230**, 489 (2004).
[15] Z. Lim, B. Maskara, F. Aguel, R. Emokpae, and L. Tung, Circulation **114**, 2113 (2006).
[16] A. Pumir and V. Krinsky, J. Theor. Biol. **199**, 311 (1999).
[17] C. Ripplinger, V. Krinsky, V. Nikolski, and I. Efimov, Am. J. Physiol. Heart. Circ. Physiol. **291**, H184 (2006).
[18] G. Beeler and H. Reuter, J. Physiol. **268**, 177 (1977).
[19] I. Efimov, V. Krinsky, and J. Jalife, Chaos **5**, 513 (1995).
[20] A. Hodgkin and A. Huxley, J. Physiol. **117**, 500 (1952).
[21] D. Noble, J. Physiol. **160**, 317 (1962).
[22] S. Matoba, T. Tetsuya, N. Keira, A. Kawahara, and K. Akashi, Circulation **99**, 817 (1999).
[23] A. Isomura, M. Hörning, K. Agladze, and K. Yoshikawa, Phys. Rev. E **78**, 066216 (2008).
[24] J. Haddad, M. L. Decker, L. C. Hsieh, M. Lesch, A. M. Samarel, and R. S. Decker, Am. J. Physiol. Cell. Physiol. **255**, C19 (1988).
[25] S. Boateng, T. Hartman, N. Ahluwalia, H. Vidula, T. Desai, and B. Russell, Am. J. Physiol. Cell. Physiol. **285**, C171 (2003).
[26] E. Entcheva and H. Bien, Biophys. Mol. Biol. **92**, 232 (2005).
[27] W. Rasband, [http://rsb.info.nih.gov/ij/] (1997–2006).
[28] R. Clayton, O. Bernus, E. Cherry, H. Dierckx, F. Fenton, L. Mirabella, A. Panfilov, F. Sachse, G. Seemann, and H. Zhang, Progress Biophys. Mol. Biol. **104**, 22 (2011).
[29] J. Keener and K. Bogar, Chaos **8**, 175 (1998).
[30] A. Kleber and C. Riegger, J. Physiol. **385**, 307 (1987).
[31] A. Kleber, C. Riegger, and M. Janse, Circ. Res. **61**, 271 (1987).
[32] B. Roth, IEEE Trans. Biomed. Eng. **4**, 326 (1997).
[33] T. Harada and A. Isomura, Prog. Theor. Phys. Suppl. **161**, 107 (2006).
[34] A. I. T. Harada and K. Yoshikawa, Physica D **237**, 2787 (2008).
[35] B. Ramza, R. Tan, T. Osaka, and R. Joyner, Circ. Res. **99**, 147 (1990).
[36] D. Noble and R. Stein, J. Physiol. **187**, 129 (1966).
[37] S. Zlochiver, V. Munoz, K. Vikstrom, S. Taffet, O. Berenfeld, and J. Jalife, Biophys. J. **95**, 4469 (2008).
[38] L. Clerc, J. Physiol. **255**, 335 (1976).
[39] D. E. Roberts, L. T. Hersch, and A. M. Scher, Circ. Res. **44**, 701 (1979).
[40] D. E. Roberts and A. M. Scher, Circ. Res. **50**, 342 (1982).
[41] P. LeGuyader, P. Savard, and F. Trelles, in *Proceeding 17th Annual Conference of the IEEE Engineering in Medicine and Biology Society, Montreal, Canada, 1995* (IEEE, 1995), p. 1739.

[42] J. Stinstra, B. Hopenfeld, and R. Macleod, Ann. Biomed. Eng. **33**, 1743 (2005).
[43] N. Bursac, Y. Loo, K. Leong, and L. Tung, Biochem. Biophys. Res. Commun. **361**, 847 (2007).
[44] S. Kidoaki and T. Matsuda, J. Biotechnol. **133**, 225 (2008).
[45] M. Hörning, S. Kidoaki, T. Kawano, and K. Yoshikawa, Biophys. J. **102**, 379 (2012).
[46] L. J. Wang and E. A. Sobie, Am. J. Physiol. Heart. Circ. Physiol. **294**, H2565 (2008).
[47] O. Bernus, R. Wilders, C. W. Zemlin, H. Verschelde, and A. V. Panfilov, Am. J. Physiol. Heart. Circ. Physiol. **282**, H2296 (2002).
[48] V. G. Fast, S. Rohr, and R. E. Ideker, Am. J. Physiol. Heart. Circ. Physiol. **278**, H688 (2000).
[49] T. Ashihara and N. A. Trayanova, Biophys. J **87**, 2271 (2004).